1 **Supporting Information**

2 **Tetra-n-butylammonium decatungstate supported on**

3 **Fe$_3$O$_4$ nanoparticles: a novel nano-catalyst for green**

4 **synthesis of nitroso compounds**

5

6 *Peng Cheng, Mohamed Sarakha, Christine Mousty, Pierre Bonnet, and Gilles Mailhot**

7 Université Clermont Auvergne, CNRS, Clermont Auvergne INP, Institut de Chimie de

8 Clermont Ferrand (ICCF) UMR 6296, BP 80026, F-63171, Aubière cedex, France

9 * Corresponding author. E-mail address: Gilles.Mailhot@uca.fr.

10 **The method of magnetite preparation**

11   A mixture of 27.03 g $FeCl_3 \cdot 6H_2O$ and 19.88 g $FeCl_2 \cdot 4H_2O$ in 800 mL Milli-Q water was

12 constantly stirred under a nitrogen atmosphere. The pH was adjusted by NaOH aqueous solution

13 to 9 - 10 and the solution volume was adjusted to 1.0 L with Milli-Q water. The reaction vessel

14 was then kept in the dark for 48 h at 60 °C. After centrifugation, the solid was carefully washed

15 with Milli-Q water until the water conductivity was less than 2.0 $\mu S\ cm^{-1}$ and then dried.

16

UV-Vis spectra of TBADT

Fig. S1 shows that TBADT at low concentration exhibits two characteristic peaks in the range of 250–350 nm in UV–vis spectra, in agreement with the previous works [1,2]. The peak at 320 nm is ascribed to oxygen to tungsten charge transition (**LMCT**) of four linear W-O-W bridge bonds in the $W_{10}O_{32}{}^{4-}$ structure [1–3] and the other weak peak at 264 nm likely corresponds to the LMCT process of the unstable structural subunit $[W_5O_{16}]^{2-}$ [4]. The molar absorption coefficient of TBADT ($W_{10}O_{32}{}^{4-}$) at 320 nm of 11983 M^{-1} cm^{-1} is in perfect agreement with the published literature data [5–7]. This can illustrate that TBADT has high purity.
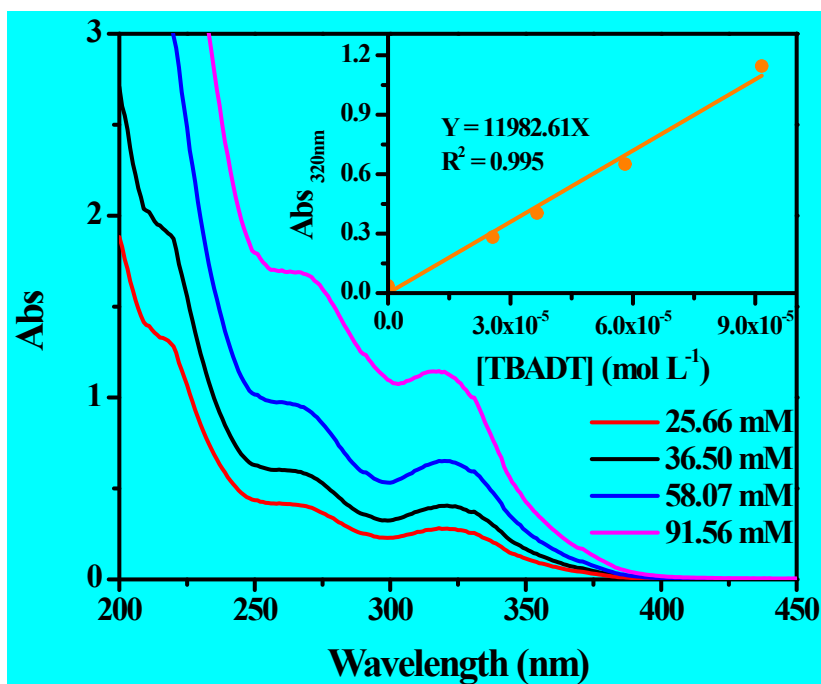
**Fig. S1.** The UV-vis spectra of different concentrations of TABDT in acetonitrile. Insert shows the calibration curve of the molar absorption coefficient of TBADT

28 **The elution conditions of preparative LC, UPLC-Ms, HPLC**

29 For **Preparative LC**. The analyses were performed using an eluent composed of acetonitrile

30 and water with 0.1 % of trifluoroacetic acid (TFA), in an isocratic mode at 25/75% and a flow

31 rate of 40 mL min^{-1}. N-SPD was finally collected after the evaporation of the solvent. For

32 **UPLC-Ms**. The elution was performed using the following gradient program: a linear increase

33 of acetonitrile from 5 to 99 % within 7.5 min followed by 0.5 min at 99 % of acetonitrile, a

34 decrease of CH_3CN to 5 % in 0.5 min, and a final step of 5 % within 3 min. The column was a

35 Kinetex EVO C18 (100 mm x 2.1 mm; particle size: 1.7 μm (Phenomenex)) and the flow rate

36 was set at 0.45 mL min^{-1}. For **HPLC.** The analyses were performed using acetonitrile as a

37 mobile phase and water with 0.5 % of phosphoric acid at a flow rate of 0.40 mL min^{-1}. The

38 elution was performed using the following gradient: 5 % of CH_3CN for 2.5 min, linear increase

39 of CH_3CN to 40 % in 4.5 min, then increase of CH_3CN to 95 % in 1.5 min, 95 % of CH_3CN for

40 1 min, and decrease of CH_3CN to 5 % in 0.5 min.

FTIR and XPS analysis of M-DT$_{2-1}$

Interactions between Fe_3O_4 and TBADT in M-DT$_{2-1}$ were investigated by FTIR. **Fig. S2** shows the FTIR spectra of TBADT (**curve a**), Fe_3O_4 (**curve b**), and M-DT$_{2-1}$ (**curve c**). The main vibration bands of TBADT (**curve a**) are observed at 992, 955, 944, and 571 cm^{-1} corresponding to the stretching vibration of the W=O$_t$ bond (O$_t$ - terminal oxygen atoms), and at 886 and 776 cm^{-1} are due to the vibrations of W-O$_b$-W (O$_b$ - corner-sharing-oxygen-bridge) and W-O$_c$-W (Oc-edge-sharing oxygen-bridge) [8]. The vibrations at a range of 2800-3000 cm^{-1} are similar to the previous study [8], which is due to e C-H bond stretching. Additionally, three characteristic vibrations resulting from TBA$^+$ at 1600 - 1100 cm^{-1} are also observed [9]. In **curve b** corresponding to the FTIR of Fe_3O_4, the band at 577 cm^{-1} can be assigned to the Fe-O stretching mode of the tetrahedral and octahedral sites [10]. The Fe–OH wide vibration band is ranged from 612 - 626 cm^{-1} [11]. By comparing the spectrum of the M-DT$_{2-1}$ with TBADT, a red shift (about 19 cm^{-1}) can be noted for the W-O$_c$-W bond (795 cm^{-1}) (**curve c**), which corresponds more likely to the interaction between TBADT and Fe_3O_4 at edge sharing oxygen-bridge. This phenomenon shows that this interaction reduces the energy of TBADT and becomes more stable.
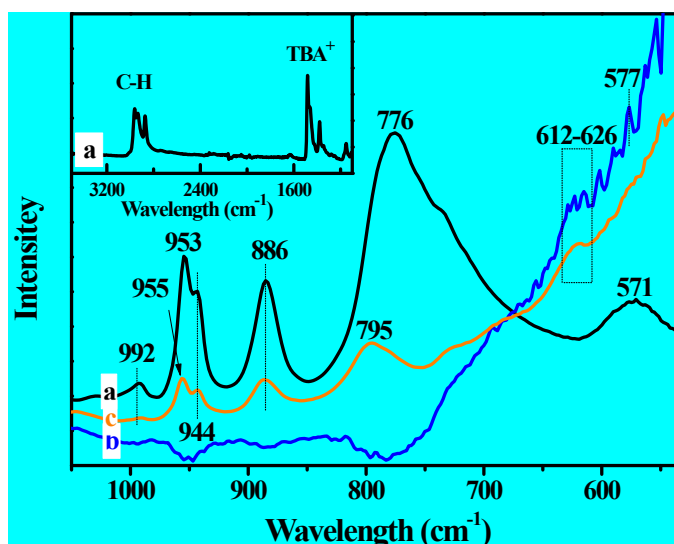
In order to reconfirm the interactions between Fe_3O_4 and TBADT and to determine the chemical compositions and electronic structure of M-DT$_{2-1}$, XPS spectra of M-DT$_{2-1}$ (before and after reaction) were compared to that of Fe_3O_4.

A typical full XPS spectrum of M-DT$_{2-1}$ (before reaction) is shown in **Fig. S3(A)**. The spectrum indicates the presence of carbon, oxygen, iron, and tungsten, arising from internal Fe_3O_4 and external TBADT. This shows that the M-DT$_{2-1}$ has no other contaminants, which is consistent with the results of XRD and FTIR. Because the atomic sensitivity factor of Fe is much higher than those of C and O, the weaker peak intensity of Fe2p implies that the Fe_3O_4 particles are uniformly and continuously coated by TBADT shells [12].

The high-resolution Fe2p spectrum of M-DT$_{2-1}$ is shown in **Fig. S3(B)**. Two peaks at 710.16 and 724.18 eV correspond to Fe2p$_{3/2}$ and Fe2p$_{1/2}$ components of Fe_3O_4, respectively [13]. The spin-orbit splitting of Fe2p peaks is broad due to a small chemical shift difference between Fe^{2+} and Fe^{3+} present in Fe_3O_4 [14]. The Fe2p$_{3/2}$ and Fe2p$_{1/2}$ spectra were both well fitted (χ^2-

73 distribution is less than 6) with two peaks. For the $Fe2p_{3/2}$ spectrum, a major peak at 711.25 eV

74 and a minor one at 709.80 eV can be ascribed to Fe^{3+} and Fe^{2+}, respectively. In addition, like

75 the $Fe2p_{3/2}$ spectrum, a major peak at 724.50 eV and a minor one at 723.09 eV were observed

76 in the $Fe2p_{1/2}$ spectrum, which can be also ascribed to Fe^{3+} and Fe^{2+}, respectively. This result

77 is in agreement with the previous study [15]. The Fe^{3+}/Fe^{2+} ratio, calculated from the

78 corresponding area under the spectrum of $Fe2p_{3/2}$ and $Fe2p_{1/2}$, is 2:1. This indicates that the

79 Fe_3O_4 is of high purity, which is consistent with the XRD result. **Table S1** shows the ratios of

80 Fe^{2+} and Fe^{3+} in Fe_3O_4 and M-DT$_{2-1}$ (before and after the reaction) and the fitting peak position

81 of Fe^{2+} and Fe^{3+} in Fe $2p_{3/2}$ and $Fe2p_{1/2}$ spectra, respectively. It can clearly be observed that the

82 Fe^{3+}/Fe^{2+} ratio and peak position in M-DT (before and after reaction) and pure Fe_3O_4 show no

83 difference. This illustrates that the chemical composition of Fe_3O_4 has not significantly changed

84 after M-DT$_{2-1}$ synthesis and after the reaction.

85 In **Fig. S3(C),** a high-resolution W4f spectrum of M-DT is exhibited. The two peaks of $W4f_{5/2}$

86 and $W4f_{7/2}$ appear at 37.01 and 34.92 eV, respectively [16], which show no difference with

87 TBADT (**Table S2**).

88 The high-resolution O1s spectrum of M-DT is shown in **Fig. S3(D)**. The O1s spectrum can

89 be divided into three components centered at 529.25, 530.00, and 531.65 eV. **Table S3** shows

90 the fitting peak position of O1s in TBADT, Fe_3O_4, and M-DT (before and after reaction). The

91 O1s peak of TBADT appears at 528.98 eV [16] and the O1s peaks of Fe_3O_4 are concentrated at

92 530.00 and 531.48 eV which correspond to Fe-O in the Fe_3O_4 phase [17,18] and the hydroxyl

93 bonding (Fe-OH) on the surface of Fe_3O_4 [18]. While in M-DT$_{2-1}$, a small shift at O1s peak of

94 W-O (increased 0.26-0.27 eV) and Fe-OH (increased 0.16-0.17 eV) can be observed (The data

95   was red bold marked in **Table S3**), comparing the peaks position of M-DT$_{2-1}$ with Fe$_3$O$_4$ and

96   TBADT. This small shift of W-O could be due to the formation of W-O-Fe interaction. The

97   Iron hydroxyl group (Fe-OH) on the surface of Fe$_3$O$_4$ can be affected by this interaction as well,

98   subsequently. This result confirms the interaction between M and DT.

99   Moreover, the small shift of the O1s spectrum in the M-DT$_{2-1}$ can still be observed after the

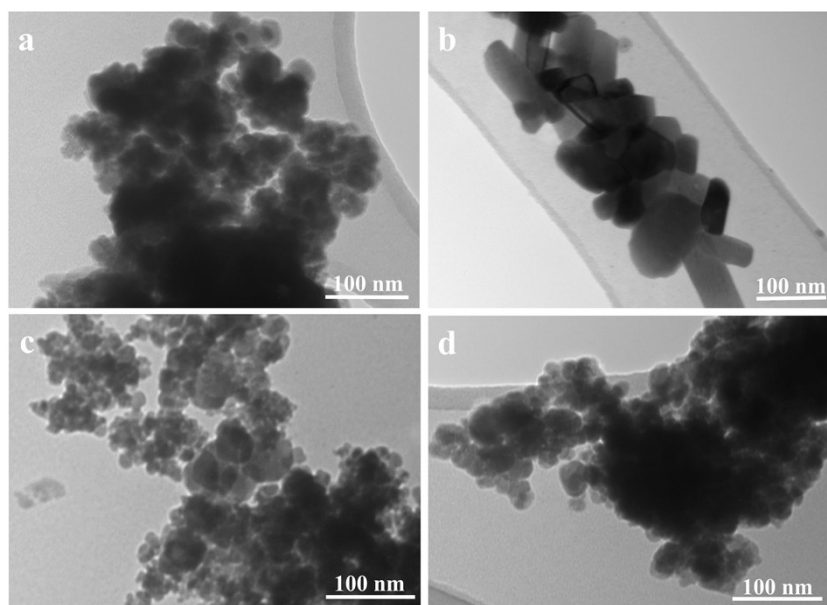100   reaction, which means this interaction is quite strong.
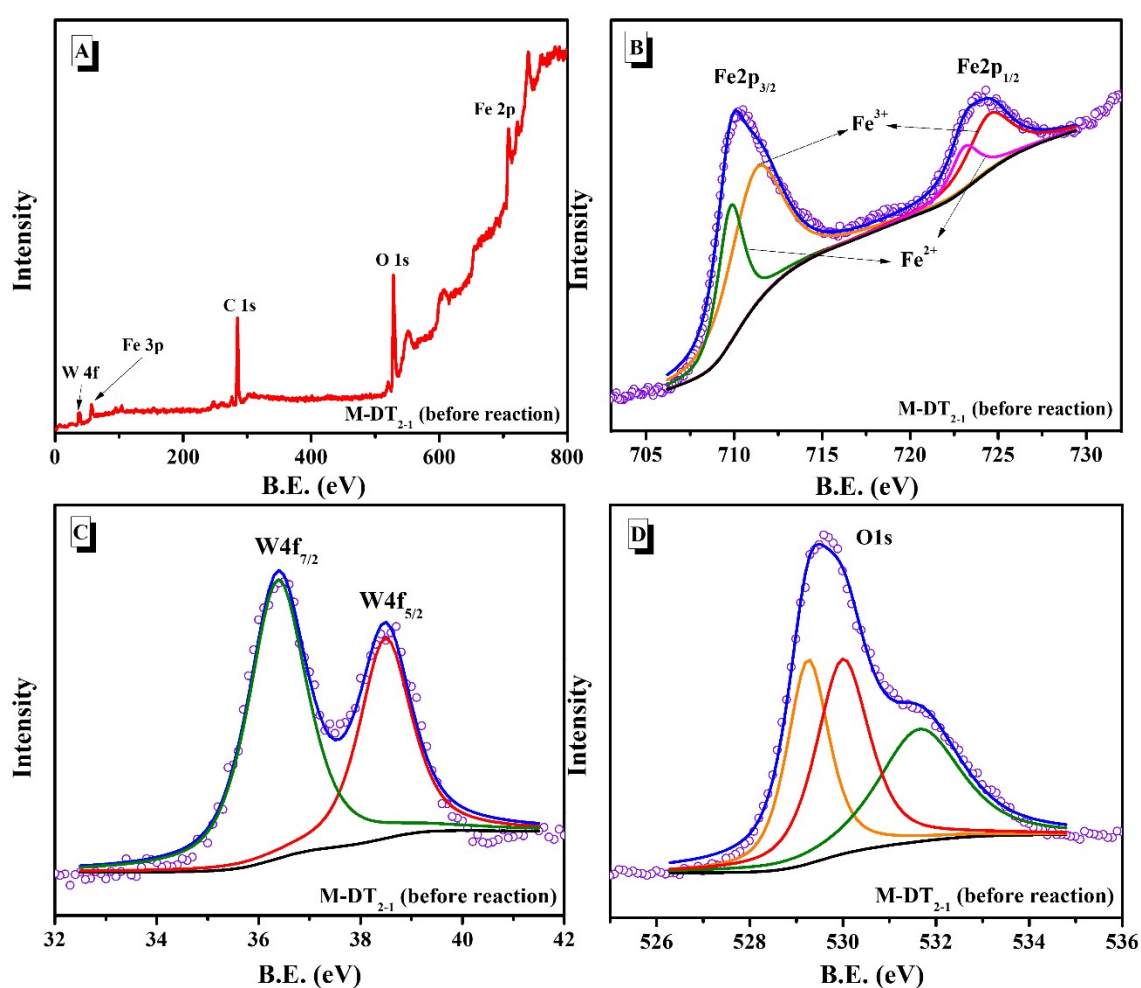
101

102   **Fig. S3.** XPS general spectra of M-DT$_{2-1}$ (A), and the high-resolution spectra of Fe2p (B),

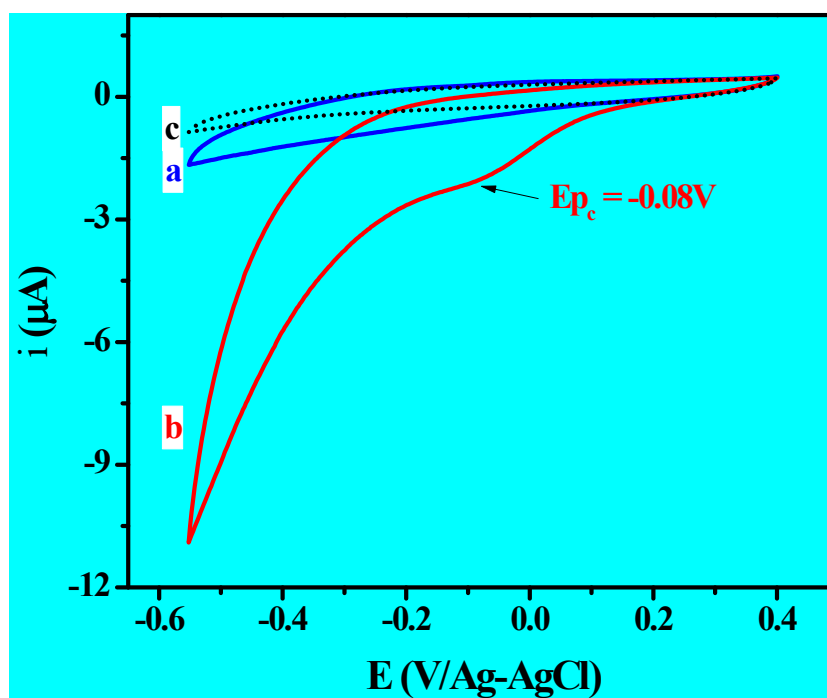103   W4f (C), and O1s (D)

9
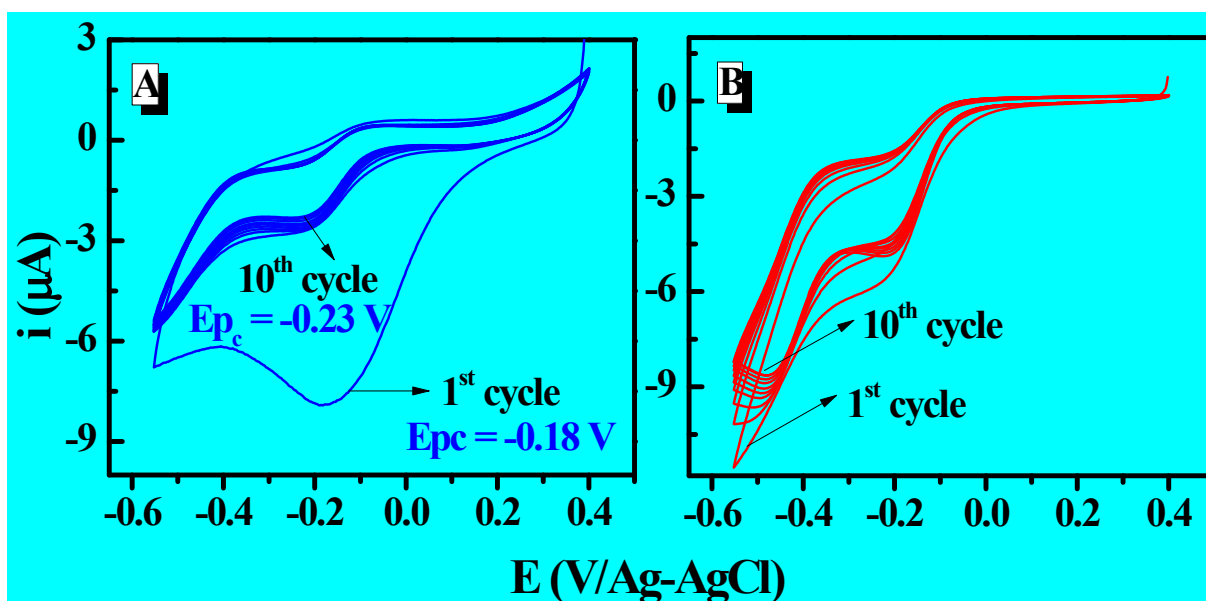
Fig. S6. Ten cycles of CVs of M-DT$_{2-1}$/PGE in the absence (A) and presence of 5 mM H$_2$O$_2$

(B) in 0.1 M LiClO$_4$ (pH = 3.5) under Ar, v = 10 mV s^{-1}.
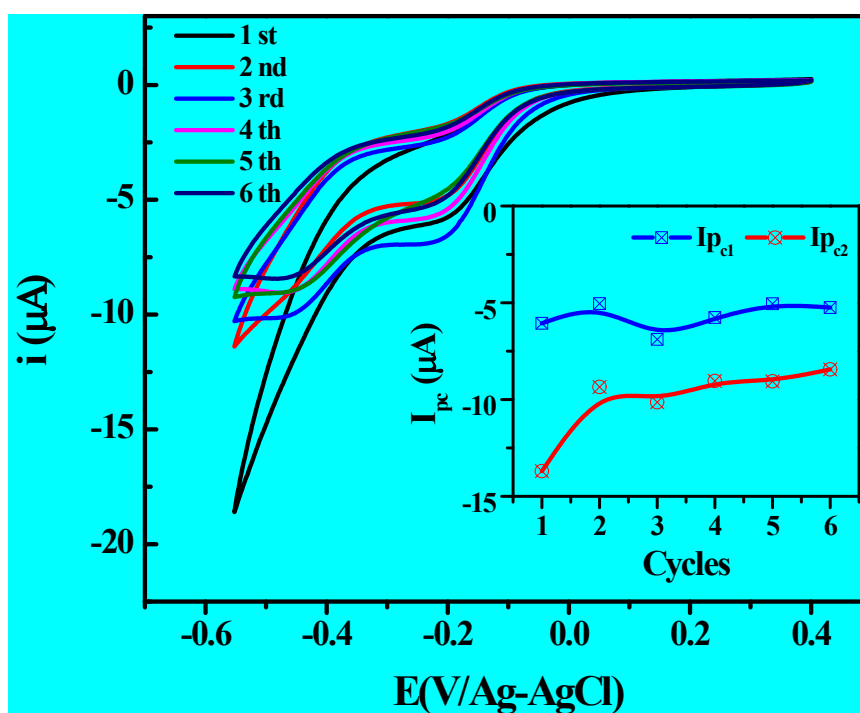
Fig. S7. Six times reuse of M-T$_{2-1}$/PGE in CVs in the presence of 5 mM H$_2$O$_2$ in 0.1 M

LiClO$_4$ (pH = 3.5) under Ar, v = 10 mV s^{-1}. Insert shows the cathodic currents Ip$_{c1}$ (⊗) and

Ip$_{c2}$ (●) at each cycle time.
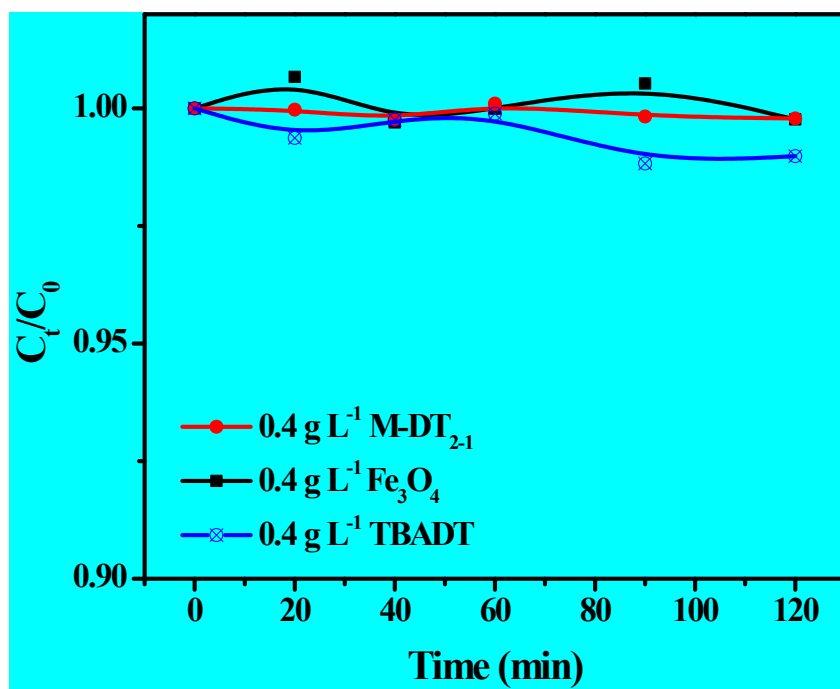
118

119   **Fig. S8.** Adsorption experiments; [SPD] = 30 µM; pH = 3.0.

120   ^{1}H NMR (500 MHz, D_2O): δ 8.22 ppm (d, J = 8.5 Hz, 2H), 8.06 ppm (d, J = 8.6 Hz, 2H),

121   7.93 ppm (d, J = 6.2 Hz, 1H), 7.90 ppm (d d d, J = 1.9, 7.3, 9.1 Hz, 1H), 7.27 ppm (d, J = 9.0

122   Hz, 1H), 7.03 ppm (t, J = 6.7 Hz, 1H). The chemical shifts and Spin coupling constants are

123   consistent with our previous work [to be published] and Castrejon et.al study [19]. After

124   normalization, the concentration of N-SPD can be obtained according to the NMR peak area.

125

126   The concentration of nitroso-sulfapyridine was calculated as following equation:

$$[\text{N - SPD}] = \frac{9A0 \times [\text{TSPd4}]}{b \times \text{Aref}} \times 1.1$$

127

128   Where [N-SPD] is the concentration of nitroso-sulfapyridine (N-SPD), A_0 is the area of nitroso-

129   sulfapyridine resonance in the 1H NMR spectrum, [TSPd$_4$] is the concentration of the reference,

130   A_{ref} is the area of reference resonance in the 1H NMR spectrum, b is the number of protons of

131   N-SPD in the signal integrated, and 9 is the number of protons resonating of TSPd$_4$ at 0 ppm.

132   The 1.1 factor came from the dilution of TSPd4. The average concentration of N-SPD

133   calculated after quantification by NMR is 52.03 μM (Dropping a sample with a chemical shift

134   of 7.93 ppm), and the relative standard deviation (RSD) is 4.8% (**Table S3**).

135

136

137
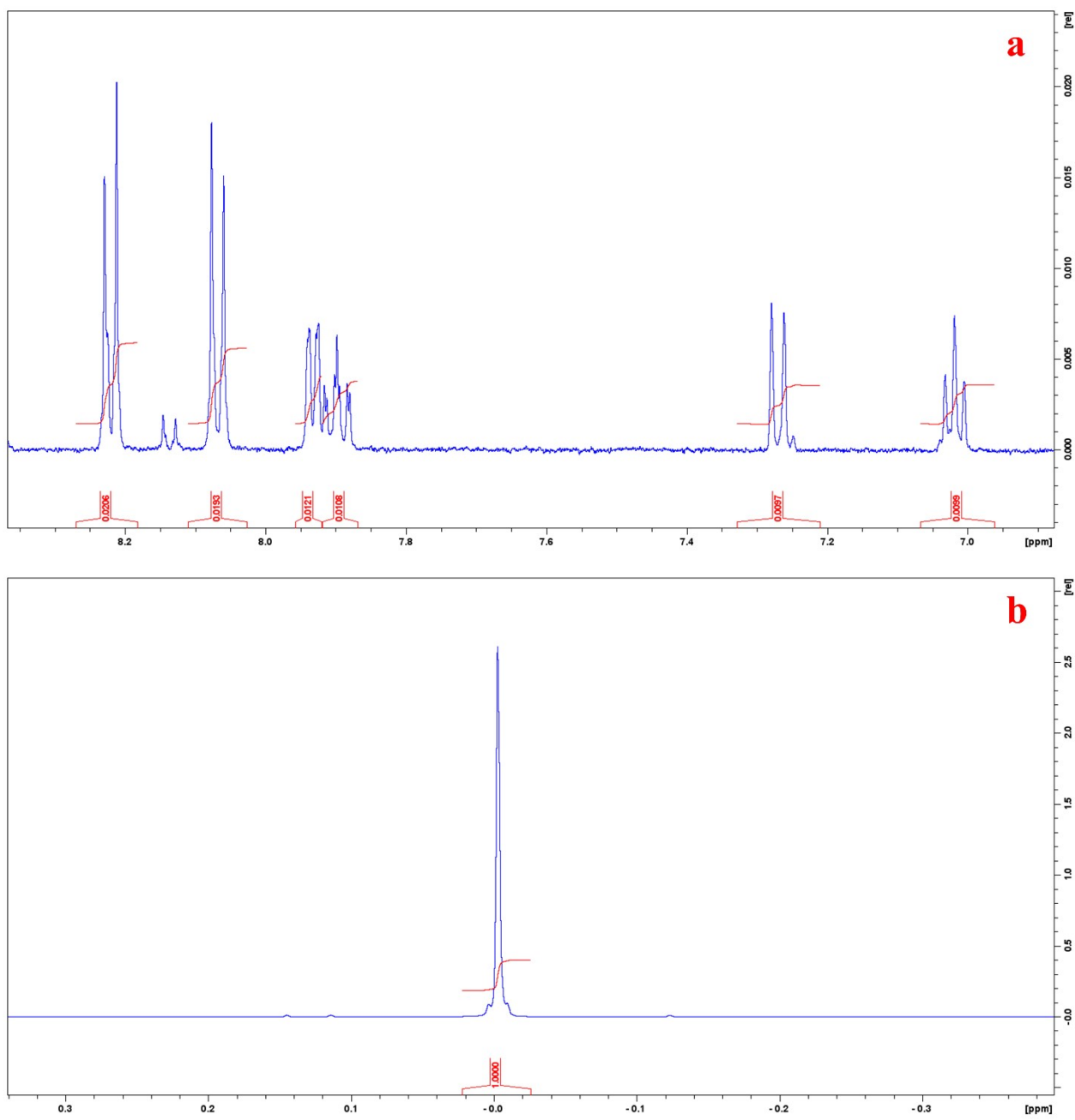
Fig. S9. NMR spectrum of N-SPD (a) and TSPd$_4$ (b)

The Effect of different parameters

a) the ratio between Fe$_3$O$_4$ and TBADT

To study the effect of the different ratios of Fe$_3$O$_4$ and TBADT on **SPD** conversion, we prepared different M-DT samples at a range of the ratio of Fe$_3$O$_4$ and TBADT from 20/1 to 2/1 (M-DT = 20/1, 10/1, 5/1 and 2/1). In **Fig. S10**, the **SPD** conversion percentage increases from 7.8 to 51.5% with the increase of the percentage of TBADT in M-DT from 4.8% to 33.3%. Under these conditions, the first-order rate constant increass from 0.69×10^{-3} to 6.3×10^{-3} min^{-1} (**Table S6**). Moreover, concerning the yield of nitroso derivative (N-SPD), **Table 3** clearly shows it remains constant at roughly 78%-86%. Such results are clearly in agreement with the fact that M-DT presents a good and interesting selectivity for the oxidation of **SPD**.

b) Effect of pH

The solution pH is a very important parameter for the selective oxidation of sulfapyridine. This was studied within the range 1.9 - 7.2 at a constant concentration of M-DT$_{2-1}$ (0.2 g L^{-1}), H$_2$O$_2$ (5.0 mM), and **SPD** (30 μM). As observed in **Fig. S11**, the efficiency of SPD conversion decreases with the increase of the solution pH. Meanwhile, the conversion percentage of SPD decreases also when the pH increases **(Table S7)**. The conversion is estimated to be around 58.9% with a rate constant of 7.31×10^{-3} min^{-1} at pH = 1.9 and 36.6% at pH = 4.0 with a rate constant of 3.66×10^{-3} min^{-1}. It drops rapidly to roughly 7.2 % at pH = 7.2 owing more likely to the lower stability of decatungstate at pH > 5.5, and also due to the interaction between Fe and W decreasing when pH increases [20]. On the other hand, the protolytic equilibrium of SPD (pKa = 8.43) may also interfere in the process leading to a change in the solution composition and

160 thus, different reaction processes occurs with the various forms of SPD. Concerning the yield

161 of N-SPD, it is estimated to be 82.55 % at pH = 2.5 and a small decrease can be observed when

162 pH = 3.0-4.6 (around 75%). While the yield of N-SPD formation is 0% at pH = 1.9, which is

163 due to the excessive oxidation of amino compounds to nitro compounds.

c) Effect of H_2O_2 concentration

165 The effect of H_2O_2 was investigated up to the concentration of 50 Mm (**Fig. S12**). As

166 observed in **Table S8,** SPD conversion percentage increases up to 36.6% (with a rate constant

167 of 3.66×10^{-3} min^{-1}) with the increase of H_2O_2 concentration up to 5.0 mM. The SPD conversion

168 percentage levels off at roughly 35% within the range of 5-20 Mm with a slight increase of the

169 rate constant that reaches 3.82×10^{-3} min^{-1}. However, for higher concentrations, a decrease of

170 the yield is observed (roughly 25 %) with a rate constant of about 2.60×10^{-3} min^{-1}. Concerning

171 the selectivity of the reaction, namely nitroso-sulfapyridine formation, its yield increases from

172 65.5% to 83.7% when H_2O_2 concentration increases from 1.0 to 20.0 mM. In addition, unlike

173 the trend of SPD conversion percentage, the yield of N-SPD remains constant at about 85%

174 when H_2O_2 concentration increases from 30.0 to 50.0 mM

d) Effect of the amount of M-DT$_{2-1}$

176 The effect of the amount of M-DT$_{2-1}$ was investigated within the range of 0 – 1.2 g L^{-1} (**Fig.**

177 **S13**). The SPD conversion percentage increases to reach 94.2% as the M-DT$_{2-1}$ concentration

178 increases from 0 to 1.2 g L^{-1} (**Table S9).** Under these conditions, the rate constant increases

179 from 2.5×10^{-3} up to 22.9×10^{-3} min^{-1}. This effect shows an interesting benefit for the oxidation

180 of SPD. Moreover, an increase of the yield for N-SPD formation is also observed (roughly

15

181 79.6% for 1.2 g L^{-1} of M-DT$_{2-1}$, indicating an important selectivity of the process under these

182 conditions.
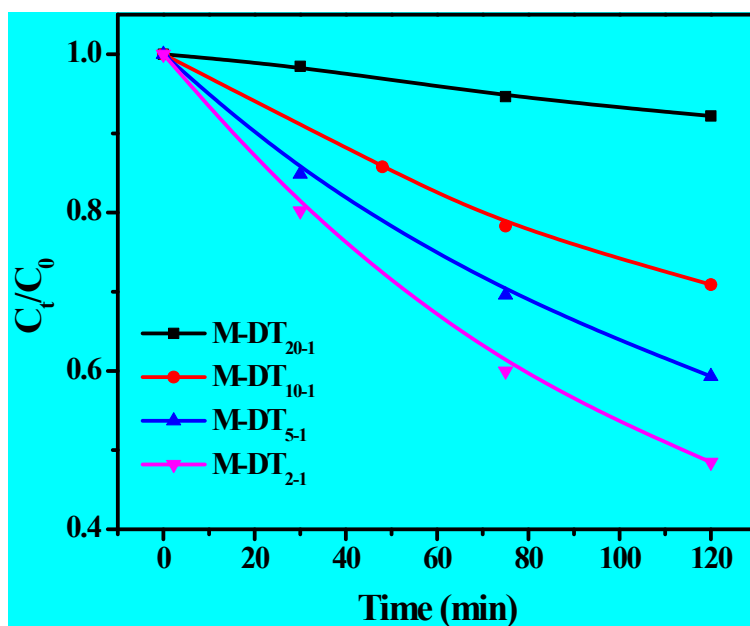
183

184 **Fig. S10.** Effect of the ratio between M and TBADT the conversion of SPD. [M-DT] = 0.2 g

185 L^{-1}, [H$_2$O$_2$] = 5.0 mM; [SPD] = 30 µM; pH = 2.5.
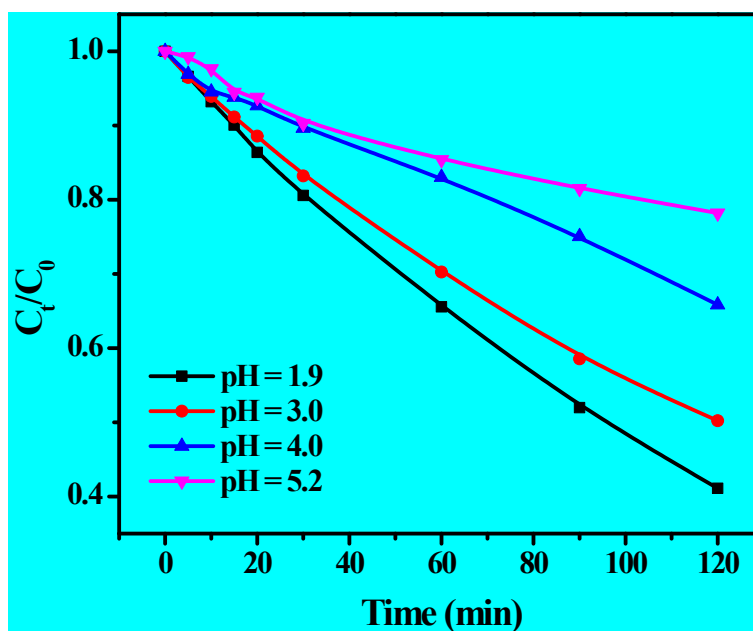
186

187 **Fig. S11.** Effect of pH on the conversion of SPD. [M-DT$_{2-1}$] = 0.2 g L^{-1}; [H$_2$O$_2$] = 5.0 mM;

188 [SPD] = 30 mM

16
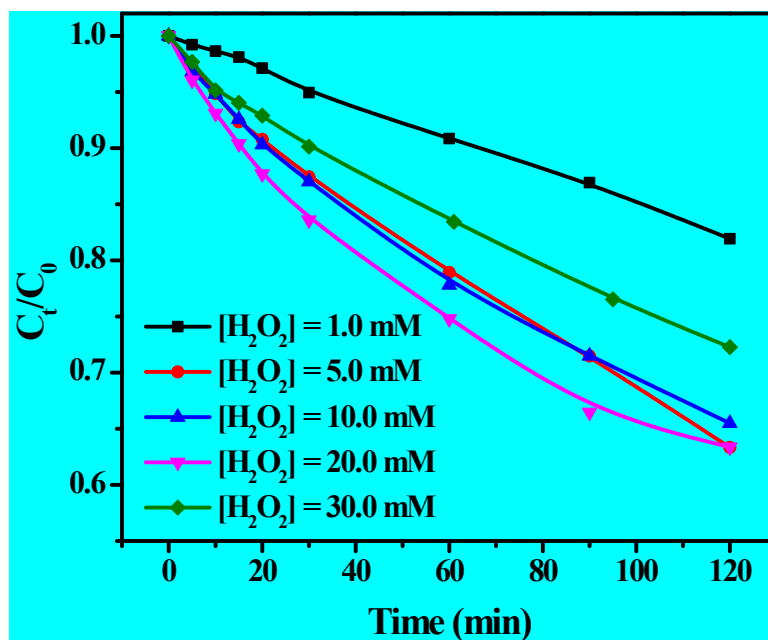
Fig. S12. Effect of H_2O_2 concentration on the conversion of SPD. [M-DT$_{2-1}$] = 0.2 g L^{-1}; [SPD] = 30 μM; pH = 4.0.
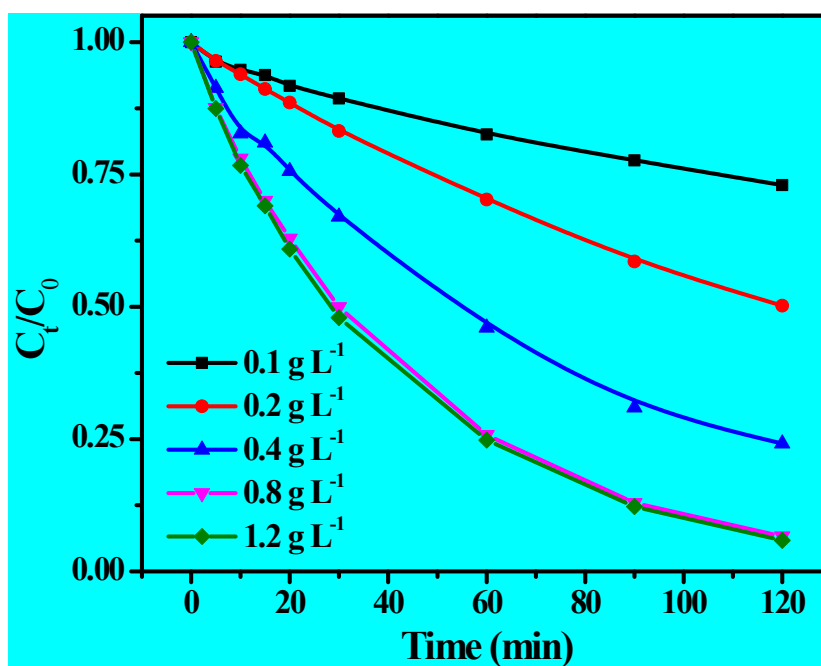
Fig. S13. Effect of the amount of M-T$_{2-1}$ on the conversion of SPD. [H_2O_2] = 5.0 mM; [SPD] = 30 μM; pH = 3.0.

17

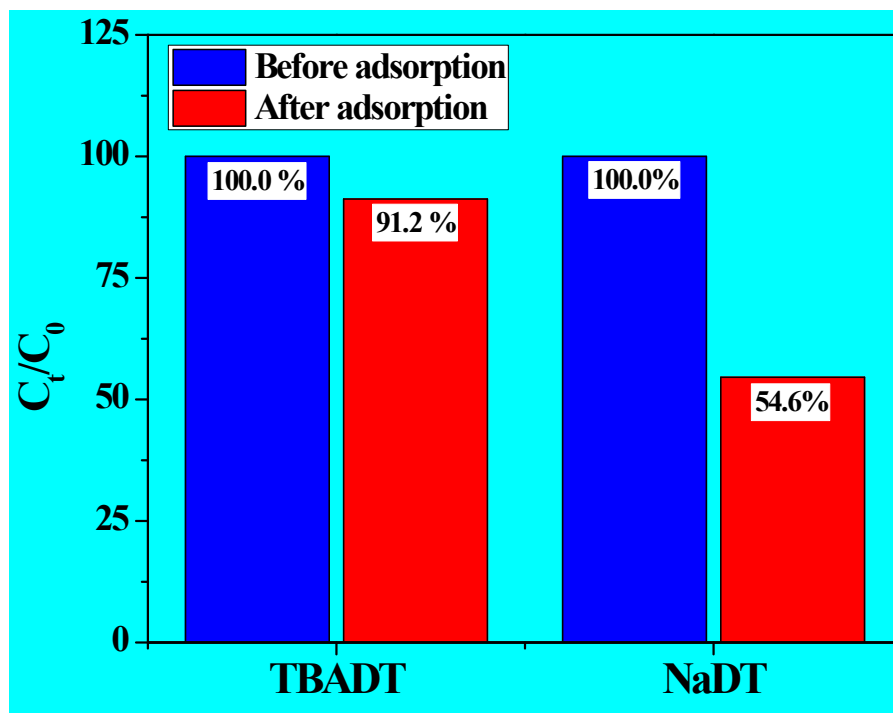**Fig. S14.** Adsorption experiment of NaDT and TBADT on magnetite surface. (NaDT and TBADT mixed with magnetite in H_2O and acetonitrile at pH 3 for 2 and 20 hours respectively.), $[Fe_3O_4]$ = 0.26 g L^{-1}, NaDT = 2.12 μmol, TBADT = 2.28 μmol.

201 **Table S1:** The ratios of Fe^{2+} and Fe^{3+} in Fe_3O_4 and M-DT$_{2-1}$ (before and after reaction) and

202 the fitting peak position of Fe^{2+} and Fe^{3+} in the Fe2p$_{3/2}$ and Fe2p$_{1/2}$ spectrum, respectively.

| Sample | Atomic ratios | | | Peak position (eV) | | | |
| | | | | Fe2p$_{1/2}$ | | Fe2p$_{3/2}$ | |
	Fe^{3+}	Fe^{2+}	χ^2	Fe^{3+}	Fe^{2+}	Fe^{3+}	Fe^{2+}
Fe_3O_4	0.668	0.332	3.74	724.46	723.05	711.29	709.83
M-DT$_{2-1}$ (before reaction)	0.667	0.333	3.18	724.50	723.09	711.25	709.80
M-DT$_{2-1}$ (after reaction)	0.667	0.333	5.70	724.44	723.03	711.25	709.79

203 χ^2 represents chi-square distribution, χ^2-distribution.

204 **Table S2** The fitting peak position of W$_{4f}$ in TBADT and M-DT before and after reaction.

| Sample | W 4f Peak position (eV) | | χ^2 |
	W 4f$_{5/2}$	W 4f$_{7/2}$	
TBADT	37.03	34.92	10.96
M-DT$_{2-1}$ (before reaction)	37.01	34.92	3.07
M-DT$_{2-1}$ (after reaction)	36.99	34.92	4.78

205 χ^2 represent chi-square distribution, χ^2-distribution.

206

207

208

209
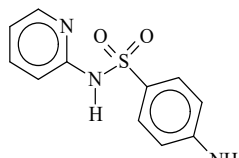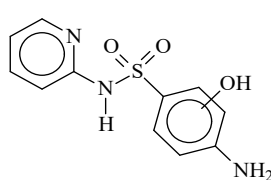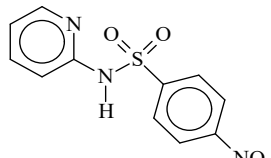
Table S3 The fitting peak position of O1s in TBADT, Fe_3O_4 and M-DT$_{2-1}$ before and after the

reaction.

Sample	O1s Peak position (eV)		
	W-O	Fe-O	Fe-OH
TBADT	528.98	-	-
Fe_3O_4	-	530.00	531.48
M-DT$_{2-1}$ (before reaction)	529.25	530.00	531.65
M-DT$_{2-1}$(after reaction)	529.24	530.00	531.64

Table S4 MS analysis of SPD products and suggested structures

R-T min	Products	M $_{measured}$ m/z	Molecular formula [M+ H]$^+$	M $_{accurate}$ m/z	Error (ppm)	Chemical structure
5.75	SPD	250.0642	$C_{11}H_{12}O_2N_3S^+$	250.0656	-0.935	
5.30	P1	266.0591	$C_{11}H_{12}O_3N_3S^+$	266.0605	-1.159	
8.03	P2	280.0384	$C_{11}H_{10}O_4N_3S^+$	280.0397	-0.832	

	P3					
8.11		264.0435	$C_{11}H_{10}O_3N_3S^+$	264.0448	-1.054	
	(N-SPD)					
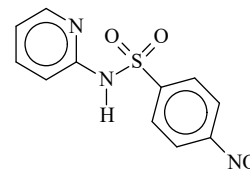
213   $[M-DT_{2-1}]$ =0.2 g L^{-1}; $[H_2O_2]$ = 5.0 mM; [SPD] = 30 μM; pH = 4.0.

214 **Tab S5** NMR information of N-SPD and TSPD$_4$

Compoud	TPSD$_4$	N-SPD					
H number	9	2	2	1	1	1	1
Chemical shift (ppm)	0.00	8.22	8.06	7.93	7.90	7.27	7.03
Normalized sum of integral	1.0000	0.0206	0.0193	0.0121	0.0108	0.0097	0.0099
Concentration (µM)	521.90	53.22	49.86	62.52	55.80	50.12	51.15
Average [N-SPD] (µM)	52.03			**RSD (%)**	4.8		

215

216 **Table S6** Effect of the ratio between Fe$_3$O$_4$ and TBADT in M-DT on SPD conversion and N-
217 SPD production within 2h

M-DT	**M-DT$_{20\text{-}1}$**	**M-DT$_{10\text{-}1}$**	**M-DT$_{5\text{-}1}$**	**M-DT$_{2\text{-}1}$**
Rate constant (min^{-1})	0.69×10^{-3}	3.00×10^{-3}	4.53×10^{-3}	6.03×10^{-3}
Conversion (%)	7.8	29.1	40.7	51.5
The yield of N-SPD formation (%)	78.6	86.3	86.0	82.6

218 [M-DT] = 0.2 g L^{-1}; [H$_2$O$_2$] = 5.0 mM; [SPD] = 30 µM; pH = 2.5

219

220

221

222

223 **Table S7** Effect of pH on SPD conversion and N-SPD production within 2h

pH	1.9	2.5	3.0	4.0	4.6	5.2	7.2
Rate constant ($\times 10^{-3}$ min^{-1})	7.30	6.03	5.84	3.66	2.09	2.07	0.68
Conversion (%)	58.9	51.5	49.8	36.6	21.9	21.8	7.2
The yield of N-SPD formation (%)	0	82.6	75.8	74.6	75.0	6.1	0

224 [M-DT$_{2-1}$] = 0.2 g L^{-1}; [H$_2$O$_2$] = 5.0 mM; [SPD] = 30 μM

225

226 **Table S8** Effect of H$_2$O$_2$ concentration on SPD conversion and N-SPD production within 2h

[H$_2$O$_2$] (mM)	0	1.0	5.0	10.0	20.0	30.0	40.0	50.0
Rate constant ($\times 10^{-3}$ min^{-1})	0	1.55	3.66	3.74	3.82	2.63	2.60	2.62
Conversion (%)	0	16.4	36.6	35.3	36.6	26.7	25.6	26.6
The yield of N-SPD formation (%)	0	65.5	74.6	74.3	83.7	85.1	85.0	84.5

227 [M-DT$_{2-1}$] = 0.2 g L^{-1}; [SPD] = 30 μM; pH = 4.0

228

229 **Table S9** Effect of M-DT$_{2-1}$ concentration on SPD conversion and yield of N-SPD within 2h

[M-DT$_{2-1}$] (g L^{-1})	0	0.1	0.2	0.4	0.8	1.2
Rate constant ($\times 10^{-3}$ min^{-1})	0	2.5	5.8	12.0	22.5	22.9
Conversion (%)	1.5	27.0	49.8	75.8	93.4	94.2
The yield of N-SPD formation (%)	0	66.2	66.8	73.8	78.7	79.6

230 [H$_2$O$_2$] = 5.0 mM; [SPD] = 30 μM; pH = 3.0

231

232 **Table S10** The comparison of catalytic performance of M-DT$_{2-1}$/H$_2$O$_2$ with previous studies

Catalyst/H$_2$O$_2$	substrate	solvent	Conversion rate (%)	Selectivity (%)	Ref
M-DT$_{2-1}$	SPD	H$_2$O	76-94	80-85	This study
Molybdenum acetylide oxo-peroxo complex	Aniline	Different Organic solvent	72-97	80-97	[21]
Au/TiO$_2$	Diffrtent aryl amines	MeOH	57-98	95	[22]
Au/Al$_2$O$_3$	p-toluidine	MeOH	16	> 95	[22]
Au/ZnO	p-toluidine	MeOH	37	> 95	[22]
Fe$_3$O$_4$@SiO$_2$–Na$_2$WO$_4$	aniline	Dimethyl carbonate	-	90	[23]

233

234 **References**

235 1 F. Bigi, A. Corradini, C. Quarantelli and G. Sartori, *Journal of Catalysis*, 2007, **250**, 222–
236   230.
237 2 A. Su, M. Chen, Z. Fu, B. Yang, J. She, F. Wan, C. Zhang and Y. Liu, *Applied Catalysis A:*
238   *General*, 2019, **587**, 117261.
239 3 S. C. Termes and M. T. Pope, *Inorg. Chem.*, 1978, **17**, 500–501.
240 4 K. Nomiya, Y. Sugie, K. Amimoto and M. Miwa, *Polyhedron*, 1987, **6**, 519–524.
241 5 D. C. Duncan, T. L. Netzel and C. L. Hill, *Inorg. Chem.*, 1995, **34**, 4640–4646.
242 6 P. Cheng, Y. Wang, M. Sarakha and G. Mailhot, *Journal of Photochemistry and*
243   *Photobiology A: Chemistry*, 2021, **404**, 112890.
244 7 D. Dondi, A. M. Cardarelli, M. Fagnoni and A. Albini, *Tetrahedron*, 2006, **62**, 5527–5535.
245 8 D. Shi, Z. Ming, Q. Wu, T. Lai, K. Zheng, C. He and J. Zhao, *Inorganic Chemistry*
246   *Communications*, 2019, **100**, 125–128.
247 9 J. Desilvestro and S. Pons, *Journal of Electroanalytical Chemistry and Interfacial*
248   *Electrochemistry*, 1989, **267**, 207–220.

249 10 S. Nasrazadani and A. Raman, *Corrosion Science*, 1993, **34**, 1355–1365.

250 11 M. Stoia, R. Istratie and C. Păcurariu, *J Therm Anal Calorim*, 2016, **125**, 1185–1198.

251 12 F. Han, L. Ma, Q. Sun, C. Lei and A. Lu, *Nano Research*, 2014, **7**, 1706–1717.

252 13 T. Radu, C. Iacovita, D. Benea and R. Turcu, *Applied Surface Science*, 2017, **405**, 337–343.

253 14 S. Tiwari, R. Prakash, R. J. Choudhary and D. M. Phase, *J. Phys. D: Appl. Phys.*, 2007, **40**,
254   4943–4947.

255 15 T. Yamashita and P. Hayes, *Applied Surface Science*, 2008, **254**, 2441–2449.

256 16 B. Yang, Z. Fu, A. Su, J. She, M. Chen, S. Tang, W. Hu, C. Zhang and Y. Liu, *Applied*
257   *Catalysis B: Environmental*, 2019, **242**, 249–257.

258 17 F. Márquez, G. M. Herrera, T. Campo, M. Cotto, J. Ducongé, J. M. Sanz, E. Elizalde, Ó.
259   Perales and C. Morant, *Nanoscale Research Letters*, 2012, **7**, 210.

260 18 E. Tanasa, C. Zaharia, I.-C. Radu, V.-A. Surdu, B. S. Vasile, C.-M. Damian and E.
261   Andronescu, *Nanomaterials*, 2019, **9**, 1384.

262 19 J. L. Castrejon, S. N. Lavergne, A. El-Sheikh, J. Farrell, J. L. Maggs, S. Sabbani, P. M.
263   O'Neill, B. K. Park and D. J. Naisbitt, *Chem. Res. Toxicol.*, 2010, **23**, 184–192.

264 20 S. Rakshit, B. Sallman, A. Davantés and G. Lefèvre, *Chemosphere*, 2017, **168**, 685–691.

265 21 A. V. Biradar, T. V. Kotbagi, M. K. Dongare and S. B. Umbarkar, *Tetrahedron Letters*,
266   2008, **49**, 3616–3619.

267 22 S. Fountoulaki, P. L. Gkizis, T. S. Symeonidis, E. Kaminioti, A. Karina, I. Tamiolakis, G.
268   S. Armatas and I. N. Lykakis, *Advanced Synthesis & Catalysis*, 2016, **358**, 1500–1508.

269 23 M. Jadidi Nejad, E. Yazdani, M. Kazemi Miraki and A. Heydari, *Chem. Pap.*, 2019, **73**,
270   1575–1583.

271